

1 **Modelling 3D permeability distribution in alluvial fans using facies architecture and** 2 **geophysical acquisitions**

3 Lin Zhu ¹, Huili Gong ¹, Zhenxue Dai ², Gaoxuan Guo ³, Pietro Teatini ⁴

4 ¹College of Resource Environment and Tourism, Capital Normal University, Laboratory Cultivation
5 Base of Environment Process and Digital Simulation, Beijing, China

6 ²Earth and Environmental Sciences Division, Los Alamos National Laboratory, Los Alamos, New
7 Mexico, United States

8 ³ Beijing Institute of Hydrogeology and Engineering Geology, Beijing, China

9 ⁴ Department of Civil, Environmental and Architectural Engineering, University of Padova, Italy

10 *Correspondence to:* Lin Zhu hi-zhulin@163.com; Huili Gong gonghl@263.com

11

12 **Abstract.** Alluvial fans are highly heterogeneous in hydraulic properties due to complex depositional
13 processes, which make it difficult to characterize the spatial distribution of the hydraulic conductivity
14 (K). An original methodology is developed to identify the spatial statistical parameters (mean, variance,
15 correlation range) of the hydraulic conductivity in a three-dimensional setting by using geological and
16 geophysical data. The Chaobai River alluvial fan in the Beijing Plain, China, is used as an example to
17 test the proposed approach. Due to the non-stationary property of the K distribution in the alluvial fan, a
18 multi-zone parameterization approach is applied to analyze the conductivity statistical properties of
19 different hydrofacies in the various zones. The composite variance in each zone is computed to describe
20 the evolution of the conductivity along the flow direction. Consistently with the scales of the
21 sedimentary transport energy, the results show that conductivity variances of fine sand, medium-coarse
22 sand, and gravel decrease from the upper (Zone 1) to the lower (Zone 3) portion along the flow
23 direction. In Zone 1, sediments were moved by higher-energy flooding, which induces poor sorting and
24 larger conductivity variances. The composite variance confirms this feature with statistically different
25 facies from Zone 1 to Zone 3. The results of this study provide insights to improve our understanding on
26 conductivity heterogeneity and a method for characterizing the spatial distribution of K in alluvial fans.

27

28 **1 Introduction**

29 Alluvial fans usually house valuable groundwater resources because of significant water storage and
30 favorable recharge conditions. Sedimentary processes forming alluvial fans are responsible for their
31 complex long-term evolution. Usually, the coarsest material (gravel) is deposited in the upper fan, with
32 the gravel passing into sand in the middle of the fan and then into silt and clay in the tail. A
33 high heterogeneity characterizes the deposit distribution because of the shifting over time of the
34 sediment-transporting streams (Zappa et al., 2006).

35 Hydraulic conductivity distributions in alluvial fans can be assigned according to the various
36 hydrofacies simulated by conditional indicator geostatistical methods (Eggleson and Rojstaczer 1998;
37 Fogg et al., 1998; Weissmann and Fogg, 1999; Weissmann et al., 2002a, 2002b; Ritzi et al., 2004, 2006;
38 Proce et al., 2004; Dai et al., 2005; Harp et al., 2008; Hinnell et al., 2010; Maghrebi et al., 2015;
39 Soltanian et al., 2015; Zhu et al., 2015a). However, the geostatistical methods require the stationary
40 assumption, i.e. the distribution of the volumetric proportions and correlation lengths of hydrofacies
41 converge to their mean values in the simulation domain. The hydrofacies and hydraulic conductivity (K)
42 distributions in alluvial fans are generally non-stationary (Weissmann et al., 1999; Anderson, 2007;
43 Weissmann et al., 2010, 2013; Zhu et al., 2016a). Hence, the use of these methods may cause large
44 characterization errors and add significant uncertainty to the predictions achieved by groundwater flow
45 and contaminant transport models (Eggleson and Rojstaczer 1998; Irving and Singha 2010; Dai et al.,
46 2014a). Zhu et al., (2016a) adopted a local-stationary assumption by dividing the alluvial fan into three
47 zones along the flow direction of the Chaobai River, China. The zones were properly detected based on

the statistical facies distribution. Then, the indicator simulation method was applied to each zone and the simulated hydrofacies distribution in the three zones was used to guide modelling the K distribution. Hydraulic conductivity of granular deposits generally varies with grain size, porosity, and sorting. Traditional methods for K estimate, e.g. well test, permeameter measurements, and grain-size analyses (Niwas et al., 2011), are very expensive, time-consuming, and make difficult to provide representative and sufficient field data for addressing spatial variations of conductivity. Recently, data fusion techniques have been developed for coupled inversion of multi-source data to estimate K distributions for groundwater numerical modeling. Geophysical data (such as surface electric resistivity and various logging data) are relatively inexpensive and can provide considerable information for characterizing subsurface heterogeneous properties (Hubbard et al., 2001; Yeh et al., 2002; Dai et al., 2004a; Morin 2006; Sikandar et al., 2010; Bevington et al., 2016). Electric resistivity data have been proven useful to derive sediment porosity distributions (Niwas and Singhal 1985; Niwas et al., 2011; Niwas and Celik 2012; Zhu et al., 2016b).

This study proposes an integrated approach to reconstruct the three-dimensional configuration of conductivity in alluvial fans by combining the hydrofacies spatial heterogeneity provided by a multi-zone transition probability model with hydrogeological and hydrogeophysical measurements, in particular resistivity loggings and electrical soundings. We assume the K distributions are local-stationary, i.e. the mean and variance of log conductivity are convergent in each hydrofacies and in each local zone. Therefore, we can compute the $\log_{10}(K)$ semivariogram in each hydrofacies and in each zone. The Chaobai alluvial fan (or called “megafan” as defined by Leier et al. (2005) and Hartley et al. (2010)

68 for very large alluvial fans) in the northern Beijing Plain, China, was selected as study area to test the
69 proposed integrated approach.

70

71 **2 Material and Methods**

72 **2.1 Study area**

73 The study area belongs to the Chaobai River alluvial fan (or megafan), in the northern Beijing Plain
74 (northern latitude 40°-40°30', eastern longitude 116°30'-117°), with an area of 1,150 km² (Fig. 1a). The
75 Chaobai River is the second largest river flowing through the Beijing Plain from north to south. The
76 ground elevation decreases southward with an average 2‰ slope. Quaternary sediments were mainly
77 deposited by flooding events with turbulent flow and consist of porous strata containing groundwater.
78 The aquifer system in the alluvial fan can be divided into three zones according to the lithological
79 features (Fig. 1): an upper fan zone (or Zone 1) with coarse sediments (e.g., sandy-gravel aquifers), a
80 middle upper fan zone (or Zone 2) where medium-coarse sediments (e.g., sandy-gravel to sandy-silt
81 aquifers) were laid down , and a fine-sediment (e.g., sand and clay multiple aquifers) middle-lower fan
82 zone (or Zone 3). Four hydrofacies, including sub-clay and clay (C), fine sand (FS), medium-coarse
83 sand (MS), and gravel (G), were classified based on the interpretations of the cores and textural
84 description of almost 700 boreholes (Zhu et al., 2015).

85 The study area is one of the most important regions for the supply of groundwater resource to Beijing.
86 The Huairou emergency groundwater resource region (hereafter EGRR) with an area of 54 Km² is
87 located in Zone 1. The total groundwater withdrawal amounted to 1.2×10⁸ m³ in 2003. Several well-

88 fields belonging to the so-called "water supply factory" were drilled along the Chaobai River in Zone 1
89 and the upper Zone 2. Most of these well-fields were built in 1979 with a designed groundwater
90 pumping volume of $1.6 \times 10^8 \text{ m}^3$ per year. The average thickness of the exploited aquifer system is
91 approximately 300 m. The long-term over-exploitation of the aquifer system has resulted in a serious
92 drawdown of water levels, which has reduced the exploitable groundwater resources and induced
93 geological disasters, mainly land subsidence, fault reactivation, and ground fissures (Cheng et al., 2015;
94 Yang et al., 2015; Zhu et al., 2015). In 2010, the annual groundwater withdrawal at the EGRR and the
95 water factory decreased to $0.86 \times 10^8 \text{ m}^3$ and $0.65 \times 10^8 \text{ m}^3$, respectively.

96 The largest cumulative land subsidence from June 2003 to January 2010 was quantified in
97 approximately 340 mm by Zhu et al., (2013, 2015) in Tianzhu County to the south. The characterization
98 of the distribution and spatial variability of the hydraulic conductivity is vital for an optimal use of the
99 limited water resources in this area.

100 **2.2 Methodological approach**

101 Nowadays, a large set of hydraulic conductivity samples can be derived by integrating appropriate
102 relations of various geological data, including hydrogeophysical measurements, borehole
103 lithostratigraphies, and hydrogeological information (total dissolved solid TDS and groundwater level).
104 These databases can be statistically processed to derive the spatial variation of $\log_{10}(K)$ for various
105 facies, including clay, fine sand, medium-coarse sand, and gravel.

106 In this paper, the statistical assessment is separately carried out for separated zones, building-up
107 experimental semivariograms that are fitted with exponential models. The optimal parameters of these

latter are estimated through a generalized output least squares (OLS) criterion. Then, the composite semivariograms are computed using a hierarchical sedimentary architecture (Ritzi et al., 2004; Dai et al., 2005) to obtain the K variance in each zone. Finally, the configuration of $\log_{10}(K)$ is simulated through a multiple-zone sequential Gaussian algorithm with estimated statistic parameters reflecting the K spatial structures in the alluvial fan. Figure 2 shows the steps involved in the developed approach.

2.3 Data set

2.3.1 Geophysical data

Geophysical data include resistivity loggings and vertical electrical soundings. There are six well-electric logs continuously recording the formation resistivity versus depth. Five logs were collected in Zone 2 and one in Zone 3. Each well log has a lithological description, which helps to relate the resistivity values to the corresponding facies.

The average resistivity of G is the largest, with a value of 198 Ω m, and that of C is the smallest with a value of 24 Ω m. Figure 3 compares the outcome of logging data in term of resistivity versus depth and the corresponding stratigraphy, where the groundwater depth is 12 m. The log was acquired in the eastern part of Zone 2. The average resistivity from 32.4 m to 40.5 m depth, where the sediments are mainly G and MS, is 70.8 Ω m. The resistivity curve shows two evident peaks from 97 m to 102 m and between 81 m and 84.5 m depth, where the MS is located.

The C resistivity is relatively low due to the good intrinsic electrical conductivity of this facies. For example from 16.5 m to 23.5 m depth, where C is the prevalent facies, a low resistivity equal to 27.2 Ω m is recorded. Since a hydrofacies with a smaller grain size has a greater total surface area, the

128 resistivity difference can partially reflect the distributions of particle sizes and the hydrofacies
129 composition. Since the obtained resistivity is the apparent resistivity, we used the resistivity located in
130 the middle of the facies block, where the resistivity is approximate to the real resistivity.

131 Vertical electrical soundings (VES) using the Schlumberger electrode configuration were carried out by
132 the Beijing Institute of Hydrogeology and Engineering Geology (BIHEG). A number of 113 detecting
133 positions were selected, with a maximum half current electrode space equal to 340 m and the potential
134 electrode space ranging from 1 to 30 m. All the sounding data (1356 VES measurements) recorded the
135 apparent resistivity of the porous medium. These data were inverted to real resistivity using the
136 nonlinear Occam inversion method (Constable et al., 1987), with a low root mean square relative error
137 of 2%. Figure 4 shows the layered structure fitting model of resistivity and the borehole lithologic
138 observations. The inversed resistivity generally reflects the difference of facies: the thick gravel layer
139 has larger resistivity while the fine sand and clay layers have relatively smaller resistivity.

140 **2.3.2 Geological and hydrogeological data**

141 Almost 700 borehole lithologic logs were collected in the study area. The sedimentary deposits show
142 large heterogeneity from the upper to the lower fan zone. In Zone 1, the dominant facies is G with a
143 volumetric proportion of 53%. The volumetric proportion of C is 16%. In Zone 2, the volumetric
144 proportion of C increases to 40%, while that of G decreases sharply to 24%. In Zone 3, the proportion
145 of G decreases further to 6% and that of C increases to 50% (Table 1). More detailed information is
146 given in Zhu et al., (2016a). The lithological information in a buffer zone of 200 m around the VES

147 locations has been used to represent the actual facies distribution in the area surrounding the sites of the
148 geophysical acquisitions.

149 A number of 35 hydrochemistry measurements with a depth from 20 m to 270 m were obtained
150 throughout the area. The minimum, maximum and average TDS values are 423 mg/l at the depth of 180
151 m, 943 mg/l at the depth of 50 m, and 692 mg/l, respectively. Generally, the TDS is very low with the
152 higher values measured in the south-western part of the study area. Because of the relatively small
153 dataset and the observed low variability, in this paper the TDS variation in the vertical direction has
154 been neglected. A TDS map was obtained by interpolating the available records using an Ordinary
155 Kriging method with a spherical semivariogram model.

156 A large number of depth of water level measurements were also collected to map the thickness of the
157 unsaturated unit. The TDS and groundwater level at each VES and resistivity log location were derived
158 from the interpolated surfaces.

159 **2.3.3 Hydraulic conductivity estimates from geophysical acquisitions**

160 The hydraulic conductivity K was estimated using the Kozeny-Carman equation:

$$161 \quad K(x, y, z) = \frac{\delta g}{\mu} \times \frac{d_{(x,y,z)}^2}{180} \frac{\phi_{(x,y,z)}^3}{(1 - \phi_{(x,y,z)})^2} \quad (1)$$

162 which is widely accepted to derive the hydraulic conductivity from grain size and porosity (Soupiou et
163 al., 2007; Utom et al., 2013; Khalil et al., 2013; Zhu et al., 2016). In Eq. (1), $d_{(x,y,z)}$ is the median grain
164 diameter (D50, mm) at location (x,y,z) , which was determined according to the lithology information, g
165 is gravity, μ the kinematic viscosity (kg/(m·s)), δ the fluid density, and $\phi_{(x,y,z)}$ the porosity. ϕ was
166 estimated using Archie's law (Eq. (2)), which relates the bulk resistivity of granular medium to porosity:

$$\rho = \alpha \rho_w \phi^{-m} s_w^{-n} \quad (2)$$

where ρ is the saturated formation resistivity (Ω m), α the pore-geometry coefficient associated with the medium ($0.5 \leq \alpha \leq 2.5$), m the cementation factor ($1.3 \leq m \leq 2.5$) (Massoud et al., 2010; Khalil and Santos 2013), s_w the water saturation, and n the saturation index. The pore fluid resistivity (Ω m) ρ_w is calculated using the following experimental relation:

$$\rho_w = \frac{5.6(\text{TDS})^b}{1 + \beta(t - 18)} \quad (3)$$

with TDS in (g/L), temperature t in ($^{\circ}\text{C}$), b and β being constant parameters (Wu et al., 2003). For the most common electrolytes, $b = -0.95$ and $\beta = 0.025$.

The logarithmically transformed values of the estimated hydraulic conductivity ($\log_{10}(K)$) were used for the geostatistical analysis because of its normal distribution (Neuman, 1990). There are 102, 2077, and 1716 conductivity samples in Zone 1, Zone 2, and Zone 3, respectively. Considering that Archie's law can only be used for clay-free granular sediments, the K values of C were not estimated in this study. Based on available information, it has been reasonably assumed that clay fraction is negligible in G, MS, and FS facies. The statistics of $\log_{10}(K)$ for the three facies in three zones are listed in Table 2. The mean $\log_{10}(K)$ values decrease from Zone 1 to Zone 3, consistently with the sedimentary transport processes in the alluvial fan. In the upper region (Zone 1), high water flowing energy made the deposits consisted mainly of larger-grained particles and the coarse-grained sediments are dominant. In the southern part (Zone 3), the deposits change to relatively fine-grained particles. The mean $\log_{10}(K)$ of gravel is greater than 2.4 ($\log(\text{m/d})$) and that of fine sand is less than 0.2 ($\log(\text{m/d})$). The lithological

information at the depth of the conductivity samples shows that volumetric proportions of FS and MS increase and that of G decreases from Zone 1 to Zone 3. The results are consistent with the statistic outputs deduced from 694 borehole data by Zhu et al., (2016a).

2.4 Statistical Methods

2.4.1 Semivariogram of hydraulic conductivity

Semivariogram describes the degree of spatial dependence of a spatial random field or stochastic process. It is a concise and unbiased characterization of the spatial structure of regionalized variables, which is important in Kriging interpolations and conditional simulations. The experimental semivariogram:

$$\hat{r}_k(h_\varphi) = \frac{1}{2N(h)} \sum_{(o,p) \in N(h)} (Y(z_o) - Y(z_p))^2 \quad (4)$$

can be fitted by an exponential model (e.g., Dai et al., 2014b):

$$r_k(h_\varphi) = \sigma^2 (1 - e^{\frac{-3h}{\lambda}}) \quad (5)$$

where $\hat{r}_k(h_\varphi)$ and $r_k(h_\varphi)$ are the experimental and model semivariograms of log conductivity Y for the k^{th} facies at a lag distance h along the φ direction. In this paper we calculate the semivariograms in the vertical and dip directions. $N(h)$ is the number of pair measuring points z_o and z_p separated by a h lag distance, σ^2 is the variance, and λ the correlation range.

The variance and range were optimized using the least-squares criterion, which was solved by the modified Gauss-Newton-Levenberg-Marquardt method (Clifton and Neuman, 1982; Dai et al., 2012). The sensitivity equation method was derived to compute the Jacobian matrix for iteratively solving the

205 gradient-based optimization problem (Samper and Neuman 1986; Carrera and Neuman 1986; Dai and
 206 Samper, 2004; Samper et al., 2006; Yang et al., 2014; Zhu et al., 2016a). The two sensitivity
 207 coefficients $\frac{\partial r_k}{\partial \sigma^2}$ and $\frac{\partial r_k}{\partial \lambda}$ are the partial derivatives of the semivariogram with respect to variance and
 208 range:

$$209 \quad \frac{\partial r_k}{\partial \sigma^2} = 1 - e^{\frac{-3h}{\lambda}} \quad (6)$$

$$210 \quad \frac{\partial r_k}{\partial \lambda} = -\sigma^2 \cdot 3h \cdot e^{\frac{-3h}{\lambda}} \cdot \lambda^{-2} \quad (7)$$

211

212 2.4.2 Composite semivariogram of log conductivity

213 Once the facies semivariograms were obtained in each zone, the composite semivariogram $\gamma(h)$ could
 214 be calculated through the following equation (e.g., Ritzi et al., 2004):

$$215 \quad \gamma(h_\varphi) = \sum_{k=1}^M \sum_{i=1}^M r_{ki}(h_\varphi) p_k t_{ki}(h_\varphi) \quad (8)$$

216 where p_k and $t_{ki}(h_\varphi)$ are the volumetric proportion of facies k and the transition probability from facies
 217 k to facies i in the φ direction with a h lag distance, respectively. Equation 8 delineates the composite
 218 semivarigoram with respect to the individual facies semivariogram and transition probability. The
 219 general shape function and range of the composite semivarigoram can be obtained from individual
 220 facies mean length and volumetric proportion with the methods described in Dai et al., (2005).

221 The transition probability $t_{ki}(h_\varphi)$ has an analytical solution as derived by Dai et al., (2007):

$$222 \quad t_{ki}(h_\varphi) = p_k + (\delta_{ki} - p_k) \cdot \exp\left(\frac{h_\varphi}{\lambda_\varphi}\right) \quad (9)$$

223 where δ_{ki} is the Kronecker delta and λ_φ is the integral scale in the direction of φ . A geostatistical
224 modeling tool GEOST (Dai et al., 2014b) modified from the Geostatistical Software Library (Deutsch
225 and Journel, 1992) and TPROGS (Carle and Fogg, 1997) was employed to compute the sample
226 transition probabilities in each zone. The parameters p_k and λ_φ were optimally estimated through a
227 modified Gauss-Newton-Levenberg-Marquardt method. More details are provided by Zhu et al.,
228 (2016a). The composite semivariograms for different zones can help us to understand the heterogeneity
229 variations from the upper to lower part of the alluvial fan, as well as the stationary property (local
230 versus regional) of the facies and hydraulic conductivity distributions.

231 **2.4.3 Sequential Gaussian simulation**

232 The Sequential Gaussian simulation (SGSIM) is a widely used stochastic simulation method to create
233 numerical model of continuous variables based on the Gaussian probability density function. The
234 process is assumed to be a stationary and ergodic random process (Deutsch and Journel, 1992;
235 Dimitrakopoulos and Luo, 2004). This method can preserve the variance and correlation range observed
236 in spatial samples. SGSIM provides a standardized normal continuous distribution of the simulated
237 variable.

238 With the assumption that the log conductivity distributions are stationary within each zone, we used
239 SGSIM simulator implemented into GEOST to model the $\log_{10}(K)$ continuous configuration under a
240 multiple-zone framework. The conductivity of the FS, MS, and G facies in each zone was simulated
241 sequentially using the structure characteristics of the semivariograms.

242 Finally, the three-dimensional conductivity configuration was derived by combining the stochastic
243 simulated facies (Zhu et al., 2016a) with the SGSIM conductivity distribution and the mean $\log_{10}(K)$ of
244 the various facies in each zone (Table 2). In detail, since each cell is characterized by specific facies and
245 zone indices, its conductivity was assigned using the corresponding (in relation to the facies and the
246 zone) 3D SGSIM outcome in that position. Since sub-clay and clay are generally characterized by a low
247 hydraulic conductivity value, a uniform K value equal to 0.0001 m/d was set to all the C cells.

248 **3 Results and Discussion**

249 **3.1 Variation of $\log_{10}(K)$ for the various facies**

250 The optimized vertical correlation range and variance of the log conductivity semivariogram (Eq. 5) are
251 listed in Table 3, along with their 95% confidence intervals. The fitting between the experimental and
252 the model semivariograms is the best in Zone 2 because of the abundant samples, while the fitting in
253 Zone 1 is the worst (Fig. 5). The fitting result of the semivariogram for the G facies is the worst in Zone
254 1. Two are the reasons: the first is the high variance of gravel in this zone; the other is the limited
255 number of samples (102 samples), which makes quite small the pair numbers within each lag spacing.
256 Hence, the computed semivariogram is highly uncertainty.

257 The variance of FS, MS, and G in the vertical direction decreases from Zone 1 to Zone 3. In the upper
258 alluvial fan, sediments were deposited under multiple water flowing events and with poor sorting. The
259 deposits consist of wide ranges of sediment categories and grain sizes. The variance of G is larger than
260 1.5, which reflects the high heterogeneity in coarse deposits. The variances of FS and MS are smaller
261 with values equal to 0.23 and 0.32, respectively. In Zone 3, these values decrease to 0.05 and 0.13,

262 respectively, with that of G sharply decreasing to 0.62. In the middle-lower fan zone, the conductivity
263 variation within each facies reduces gradually because the ground surface slope becomes smaller or flat,
264 the sediment transport energy decreases, and the deposits within the three facies are well sorted.

265 Note that the ranges are correlated with the facies structure parameters such as the indicator correlation
266 scale, mean thickness (or length), and volumetric proportion (Dai et al., 2004b; 2007). The estimated
267 correlation ranges of FS, MS and G along the vertical direction in Zone 1 do not show big difference
268 with values equal to 6.0 m, 8.0 m and 6.5 m, respectively. Zone 2 was extended from the fan apex zone
269 (Zone 1) with much larger area, which allows for greater preservation potential of finer sediments (such
270 as medium-coarse sand (MS), fine sand (FS), and clay or sub clay (C)) than the more proximal Zone 1.
271 Therefore, in Zone 2 the volumetric proportions for these three facies increase while that of gravel
272 decreases. The estimated ranges of G and MS are increased, respectively. In Zone 3, the range
273 difference among the three facies decreases gradually. The range of FS is about 6.0 m, which is twice as
274 much as that of MS. The spatial variation of the structure parameters of three facies causes the large
275 changes of the correlation ranges from Zone 1 to Zone 3.

276 Due to the small number of conductivity samples in Zone 1, the variance of $\log_{10}(K)$ along the dip
277 direction is calculated only in Zone 2 and Zone 3 (Table 4, Fig. 6). The variances of G, MS and FS in
278 Zone 2 are higher than those in Zone 3, as observed along the vertical direction. This occurrence
279 possibly reflects that the water flow and sediment transport energy decrease along the original flow
280 direction. Lower energy flow in Zone 3 cause better sediment sorting and weak heterogeneity (or lower
281 variance) in hydraulic conductivity.

282 **3.2 Compositd semivariogram of $\log_{10}(K)$**

283 The composite semivariogram in the vertical direction at each zone is calculated by Eq. (8), using the
284 volume proportions (Table 1) and transition probability (Eq. (9)) with the same values of the lag
285 distance used to compute the facies semivariograms (Fig. 7). The values of the optimized variance are
286 0.68, 0.11, and 0.03 in Zone 1, Zone 2, and Zone 3, respectively. The high flow energy and the large
287 number of flooding events contributing to sediment deposition are the main causes of the high
288 heterogeneity (largest variance) of the deposits in the upper part of the alluvial fan. The changes of
289 variance between the three zones support the utilization of the local-stationary assumption and
290 simulation of multiple-zone based conductivity distributions for the Chaobai alluvial fan.

291 **3.3 Configuration of $\log_{10}(K)$**

292 The configuration of $\log_{10}(K)$ in three dimensions is showed in Fig.8. The distribution of conductivity is
293 generally consistent with that of the facies. The conductivity of large grain-size sediments is generally
294 larger, thus on the average K is much larger in the upper zone than in the lower part of the alluvial fan.
295 The regions with high conductivity (red color in Fig. 8) in Zone 1 are more continuous than that in other
296 parts. The adjacent cells with the smallest conductivity (blue color in Fig. 8) are obviously located
297 mainly in Zone 3. The mean conductivity is smaller in the southern part of the study area, where the
298 piezometric drawdowns in the multi-layer aquifer system were larger and the surface subsidence more
299 serious (Zhu et al., 2013, 2015). Note that since we simulated the dip direction along one orientation
300 (along the main water flow direction), the simulated facies in the fan apex did not show a radiating

301 pattern. More information about simulating the radiating pattern can be found from Carle et al. (1997)
302 and Fogg et al. (1998).

303 Based on the three dimensional K configuration, the average value of K in the depth range from 0 m to
304 300 m amounts to 194 m/d, 25 m/d and 4 m/d in Zone 1, Zone 2, and Zone 3, respectively. These values
305 are comparable with those provided by the Beijing Institute of Hydrogeology and Engineering Geology
306 (2007) based on a number of pumping tests carried out over several years in the study area. In this
307 BIHEG report the average value of K is >300 m/d in Zone 1, between 30 and 100 m/d in Zone 2, and
308 <30 m/d in Zone 3 (Fig. 1b). The fact that our average K values are gently smaller than these latter are
309 likely due to the fact that the outcome of pumping tests are generally more representative of coarser
310 sediments. Conversely, those estimated from the stochastic framework represent more properly the
311 heterogeneous distributions of the hydraulic conductivity (Zhu et al., 2016b).

312 Investigating the stochastic results along the vertical direction, it is interesting to notice that the average
313 K in deep units of Zone 1 and Zone 2 is smaller than that in the shallow strata. For example, in Zone 1
314 the average K for the cells from 0 m to 100 m deep is 295 m/d, which is three times as much the value
315 for the depth range between 200 m and 300 m. Conversely, no significant variation of K versus depth is
316 observed in Zone 3, with only a small decrease of the average K from the deeper to the shallower units.

317 **4 Conclusions**

318 This paper proposes a geostatistical method under a multiple zone framework, properly supported by a
319 large number of geophysical investigations, to detect the distribution and the related variance of the
320 hydraulic conductivity in three-dimensional domains. In particular, the optimized statistical parameters

(e.g., log conductivity variance and correlation range) of semivariograms are estimated using the modified Gauss-Newton-Levenberg-Marquardt method. The Chaobai alluvial fan is used as a case study area. Multiple data including downhole resistivity logging data, vertical electric soundings, well-bore lithologic logs, TDS measurements, and depths to the water table are integrated to derive a dataset of conductivity values in a three-dimensional setting. Log conductivity semivariograms fitted with exponential functions were constructed for three facies, including fine sand, medium-coarse sand and gravel, in each of the three zones into which the Chaobai fan is divided to guarantee local stationarity of the statistical process. The composite semivariogram of the three facies has been derived for the two zones where a sufficiently large number of samples are available. The $\log_{10}(K)$ configuration is simulated using the sequential Gaussian simulation model based on statistic parameters of $\log_{10}(K)$ and the structure suggested by a 3D hydrofacies simulation.

For the specific test case, the variance along the vertical direction of fine sand, medium-coarse sand, and gravel decreases from the upper part of the alluvial fan, where the values amount to 0.23, 0.32, and 1.60, to the lower portion of the Chaobai fan with values of 0.05, 0.126, and 0.62, respectively. This behavior reflects the higher transport energy in the upper alluvial fan that causes a poor sediment sorting. In the middle alluvial fan, the transport energy decreases and the sediments tend to be relatively well-sorted. The variance of the gravel is larger than that of other lithologies. The different flow energy significantly affected the coarse sediments in the vertical direction. Along the dip direction, the variance of three facies (gravel, medium-coarse sand and fine sand) in the middle fan is larger than that in the lower fan. The composite variance of $\log_{10}(K)$ in the vertical direction shows that the large heterogeneity in the upper fan (with a value of 0.68) decreases in the lower zone.

342 The distribution of hydraulic conductivity is consistent with that of the facies. Hydraulic conductivity is
343 much larger in the upper zone than that in the lower part of the alluvial fan. This result provides
344 valuable insights for understanding the spatial variations of hydraulic conductivity and setting-up
345 groundwater flow, transport, and land subsidence models in alluvial fans.

346 Concluding, it is worth highlighting that we depicted an original method to detect the variance and
347 configuration of conductivity by fusing multiple-source data in three-dimensional domains. The
348 proposed approach can be easily used to statistically characterize the hydraulic conductivity of the
349 various alluvial fans that worldwide are strongly developed to provide high-quality water resources. We
350 are aware of some restrictions in the dataset available at the date for the Chaobai alluvial fan, for
351 example the assumed uniform distribution of TDS versus depth and the relatively small number of the
352 conductivity samples in the upper fan zone. Nonetheless, the proposed methodology will be re-applied
353 in the near future as soon as new information will become available, thus allowing to improve the
354 estimation accuracy of spatial statistics parameters and the configuration of hydraulic conductivity in
355 this Quaternary system so important for the Beijing water supply.

356 **Data availability**

357 The geophysical measurements, borehole lithostratigraphies, and hydrogeological information in the
358 north part of Beijing Plain can be partly accessible by contacting Beijing Institute of Hydrogeology and
359 Engineering Geology.

360 **Author contribution**

361 Lin Zhu, Huili Gong and Zhenxue Dai derived the method of spatial variance and 3D configuration of

conductivity, performed data analysis and wrote the draft manuscript. Gaoxuan Guo collected the geological and geophysical data, discussed the results. Pietro Teatini discussed the results, reviewed and revised the manuscript.

Competing interests

The authors declare that they have no conflict of interest.

Acknowledgements

This work was supported by the National Natural Science Foundation (No.41201420, 41130744) and Beijing Nova Program (No.Z111106054511097). Pietro Teatini was partially supported by the University of Padova, Italy, within the 2016 International Cooperation Program.

References

- Anderson, M.P.: Introducing groundwater physics, *Phys. Today*, 42–47, 2007
- Beijing Institute of Hydrogeology and Engineering Geology: Groundwater flow model and the potential groundwater resources in Beijing Plain, Internal Report, 60-64., 2007 (In Chinese)
- Bevington, J., Piragnolo, D., Teatini, P., Vellidis, G., and Morari, F.: On the spatial variability of soil hydraulic properties in a Holocene coastal farmland, *Geoderma*, 262: 294-305, doi:10.1016/j.geoderma.2015.08.025, 2016.
- Carle, S.F., and Fogg, G.E.: Modeling spatial variability with one and multimensional continuous-lag Markov chain, *Math. Geol.*, 29: 891-918, doi: 10.1023/a:1022303706942, 1997.
- Carrera, J., and Neuman, S.P.: Estimation of aquifer parameters under steady state and transient condition: 2. Uniqueness, stability, and solution algorithms, *Water Resour. Res.*, 22, 211 – 227, doi: 10.1029/wr022i002p00211, 1986.

383 Cheng, G., Wang, H., Luo, Y., and Guo, H.: Study of the deformation mechanism of the Gaoliying
 384 ground fissure: Prevention and Mitigation of Natural and Anthropogenic Hazards due to Land
 385 Subsidence - Proc. IX Int. Symp. on Land Subsidence, K. Daito et al. eds., Proc. IAHS, UK, 231-234,
 386 2015.

387 Clifton, P.M., and Neuman, S.P.: Effects of kriging and inverse modeling on conditional simulation of
 388 the Avra Valley aquifer in southern Arizona, *Water Resour. Res.*, 18, 1215-1234, doi:
 389 10.1029/wr018i004p01215, 1982.

390 Constable, S.C., Parker, R.L., and Constable, C.G.: Occam's inversion: A practical algorithm for
 391 generating smooth models from electromagnetic sounding data, *Geophysics*, 52, 289-300, 1987.

392 Dai, Z., and Samper, J.: Inverse problem of multicomponent reactive chemical transport in porous
 393 media: Formulation and applications, *Water Resour. Res.*, 40, W07407, doi: 10.1029/2004wr003248,
 394 2004.

395 Dai, Z., Ritzi, R., and Dominic, D.: Estimating parameters for hierarchical permeability correlation
 396 models. Aquifer Characterization, Bridge, J.S. and Hyndman, D.W. *SEPM Society for Sedimentary*
 397 *Geology*, USA, 41-54, doi: 10.2110/pec.04.80.0041, 2004a.

398 Dai, Z., Ritzi, R., Huang, C., Dominic, D., and Rubin, Y.: Transport in heterogeneous sediments with
 399 multimodal conductivity and hierarchical organization across scales, *J. of Hydrol.*, 294, 68-86, doi:
 400 10.1007/s00477-014-0922-3, 2004b.

401 Dai Z., Ritzi, R., and Dominic, D.: Improving permeability semivariograms with transition probability
 402 models of hierarchical sedimentary architecture derived from outcrop analog studies. *Water Resour.*
 403 *Res.*, 14 W07032, doi: 10.1029/2004wr003515, 2005.

404 Dai, Z., Wolfsberg, A., Lu, Z., and Ritzi, R.: Representing aquifer architecture in macrodispersivity
 405 models with an analytical solution of the transition probability matrix. *Geophys. Res. Lett.*, 34, L20406,
 406 doi: 10.1029/2007GL031608, 2007.

407 Dai, Z., Wolfsberg, A., Reimus, P., Deng, H., Kwicklis, E., Ding, M., Ware, D., and Ye, M.:
 408 Identification of sorption processes and parameters for radionuclide transport in fractured rock, *J.*
 409 *Hydrol.*, 414-415, 220-230, doi: 10.1016/j.jhydrol.2011.10.035, 2012.

410 Dai, Z., Viswanathan, H., Fessenden-Rahn, J., Middleton, R., Pan, F., Jia, W., Lee, S., McPherson, B.,
 411 Ampomah, W., and Grigg, R.: Uncertainty quantification for CO₂ sequestration and enhanced oil
 412 recovery, *Energy Procedia*, 63, 7685–7693, 2014a.

413 Dai, Z., Middleton, R., Viswanathan, H., Fessenden-Rahn, J., Bauman, J., Pawar, R., Lee, S., and
 414 McPherson, B.: An integrated framework for optimizing CO₂ sequestration and enhanced oil recovery.
 415 *Environ. Sci. Technol. Lett.*, 1, 49-54, doi: 10.1021/ez4001033, 2014b.

416 Deutsch, C.V., and Journel, A.G. GSLIB: Geostatistical software library, Oxford Univ. Press. New
 417 York, 340, 1992.

418 Dimitrakopoulos, R., and Luo, X.: Generalized sequential Gaussian simulation on group size v and
 419 screen-effect approximations of large field simulations. *Math. Geol.*, 36, 567-590, doi:
 420 10.1023/b:matg.0000037737.11615.df, 2004.

421 Eggleston, J., and Rojstaczer, S.: Identification of large-scale hydraulic conductivity trends and the
 422 influence of trends on contaminant transport. *Water Resour. Res.*, 34, 2155-2186, doi:
 423 10.1029/98wr01475, 1998.

424 Fogg, G.E., Noyes, C.D., and Carle, S.F.: Geologically based model of heterogeneous hydraulic
 425 conductivity in an alluvial setting, *Hydrogeol. J.*, 6(1), 131-143, doi: 10.1007/s100400050139, 1998.

426 Harp, D., Dai, Z., Wolfsberg, A., and Vrugt, J.: Aquifer structure identification using stochastic
 427 inversion, *Geophys. Res. Lett.*, 35, L08404, doi: 10.1029/2008gl033585, 2008.

428 Hartley, A.J., Weissmann, G.S., Nichols, G.J., and Warwick, G.L., Distributive fluvial systems:
 429 characteristics, distribution, and controls on development, *J. of Sediment. Res.*, 79, 167-183, doi:
 430 10.2110/jsr.2010.016, 2010.

431 Hinnell, A.C., Ferre, T.P.A., Vrugt, J., Huisman, J.A., Moysey, S., Rings, J., and Kowalsky, M.B.:
 432 Improved extraction of hydrologic information from geophysical data through coupled
 433 hydrogeophysical inversion. *Water Resour. Res.*, 46, doi: 10.1029/2008wr007060, 2010.

434 Hubbard, S.S., Chen, J.S., Peterson, J., Majer, E.L., Williams, K.H., Swift, D.J., Mailloux, B., and
 435 Rubin, Y.: Hydrogeological characterization of the South Oyster Bacterial Transport site using
 436 geophysical data, *Water Resour. Res.*, 37, 2431-2456, doi: 10.1029/2001wr000279, 2001.

437 Irving, J., and Singha, K.: Stochastic inversion of tracer test and electrical geophysical data to
 438 estimate hydraulic conductivities, *Water Resour. Res.*, 46, W11514, doi: 10.1029/2009WR008340, 2010.

439 Khalil, M.A., and Santos, F.A.M.: Hydraulic conductivity estimation from resistivity logs: a case study
 440 in Nubian sandstone aquifer. *Arab. J. Geosci.*, 6, 205-212. doi: 10.1007/s12517-011-0343-2, 2013.

441 Leier, A.L., P. G. DeCelles, J. D. Pelletier, Mountains, monsoons, and megafans, *Geology*, 33, 289-292.
 442 doi: 10.1130/G21228.1, 2005.

443 Maghrebi, M., Jankovic, I., Weissmann, G.S., Matott, L.S., Allen-King, R.M., and Rabideau, A.J.,
 444 Contaminant tailing in highly heterogeneous porous formations: Sensitivity on model selection and
 445 material properties. *J. of Hydrol.*, 531, 149-160. doi: 10.1016/j.jhydrol.2015.07.015, 2015.

446 Massoud, U., Santos, F.A.M., Khalil, M. A., Taha, A., and Abbas, A. M.: Estimation of aquifer
 447 hydraulic parameters from surface geophysical measurements: a case study of the Upper Cretaceous
 448 aquifer, central Sinai, Egypt, *Hydrogeol. J.*, 18, 699-710, doi: 10.1007/s10040-009-0551-y, 2010.

449 Morin, R.H.: Negative correlation between porosity and hydraulic conductivity in sand-and-gravel
 450 aquifers at Cape Cod, Massachusetts, USA, *J. Hydrol.*, 316, 43-52, doi:10.1016/j.jhydrol.2005.04.013,
 451 2006.

452 Neuman, S.P.: Universal scaling of hydraulic conductivities and dispersivities in geologic media, *Water*
 453 *Resour. Res.*, 26, 1749-1758, 1990.

454 Niwas, S., and Singhal, D.C.: Aquifer transmissivity of porous media from resistivity data, *J. Hydrol.*,
 455 82, 143-153, doi: 10.1016/0022-1694(85)90050-2, 1985.

456 Niwas, S., Tezkan, B., and Israil, M.: Aquifer hydraulic conductivity estimation from surface
 457 geoelectrical measurements for Krauthausen test site, Germany, *Hydrogeol. J.*, 19, 307-315, doi:
 458 10.1007/s10040-010-0689-7, 2011.

459 Niwas, S., and Celik, M.: Equation estimation of porosity and hydraulic conductivity of Ruhrtal aquifer
 460 in Germany using near surface geophysics. *J. Appl. Geophys.*, 84, 77-85, doi:
 461 10.1016/j.jappgeo.2012.06.001, 2012.

462 Proce, C., Ritzi, R. W., Dominic, D., and Dai, Z.: Modeling multiscale heterogeneity and aquifer
 463 interconnectivity, *Ground Water*, 42, 658-670, 2004.

464 Ritzi R., Dai, Z., Dominic, D., Rubin Y.: Reply to comment by Shlomo P. Neuman on “Spatial
 465 correlation of permeability in cross-stratified sediment with hierarchical architecture”. *Water Resour.*
 466 *Res.*, 42, W05602, doi:10.1029/2005WR004402, 2006.

467 Ritzi R., Dai, Z., and Dominic, D.: Spatial correlation of permeability in cross-stratified sediment with
 468 hierarchical architecture. *Water Resour. Res.*, 40, W03513, doi: 10.1029/2003wr002420, 2004.

469 Samper, F.J., and Neuman, S.P.: Adjoint state equations for advective-dispersive transport: Proceeding
 470 of the 6th International Conference in Finite Elements in Water Resource, 423-437, New York, doi:
 471 10.1007/978-3-662-11744-6_31, 1986.

472 Samper, J., Dai, Z., Molinero, J., García-Gutiérrez, M., Missana, T., and Mingarro, M.: Inverse
 473 modeling of tracer experiments in FEBEX compacted Ca-bentonite. *Physics and Chemistry of the Earth*,
 474 31, 640-648, 2006.

475 Sikandar, P., Bakhsh, A., Arshad, M., and Rana, T.: The use of vertical electrical sounding resistivity
 476 method for the location of low salinity groundwater for irrigation in Chaj and Rachna Doabs, *Environ.*
 477 *Earth Sci.*, 60, 1113-1129, doi: 10.1007/s12665-009-0255-6, 2010.

478 Soltanian, M.R., Ritzi, R.W., Huang, C.C., and Dai, Z.: Relating reactive solute transport to hierarchical
 479 and multiscale sedimentary architecture in a Lagrangian-based transport model: 2: Particle displacement
 480 variance. *Water Resour. Res.*, 51, 1601-1618, doi: 10.1002/2014wr016354, 2015.

481 Soupios, P.M., Kouli, M., Vallianatos, F., Vafidis, A., and Stavroulakis, G.: Estimation of aquifer
482 hydraulic parameters from surficial geophysical methods: A case study of Keritis Basin in Chania
483 (Crete-Greece), *J. Hydrol.*, 338, 122-131, doi: 10.1016/j.jhydrol.2007.02.028, 2007.

484 Utom, A.U., Odoh, B.I., Egboka, B.C.E., Egboka, N.E., and Okeke, H.C.: Estimation of subsurface
485 hydrological parameters around Akwuke, Enugu, Nigeria using surface resistivity measurements. *J.*
486 *Geophys. Eng.*, 10, 025016, doi: 10.1088/1742-2132/10/2/025016, 2013.

487 Weissmann, G.S., and Fogg, G.E.: Multi-scale alluvial fan heterogeneity modeled with transition
488 probability geostatistics in a sequence stratigraphic framework. *J. Hydrol.*, 226, 48–65, doi:
489 10.1016/S0022-1694(99)00160-2, 1999.

490 Weissmann, G.S., S.F. Carle, G.E. Fogg, Three-dimensional hydrofacies modeling based on soil
491 surveys and transition probability geostatistics, *Water Resour. Res.*, 35(6), 1761–1770, 1999.

492 Weissmann, G.S., Yong, Z., Fogg, G.E., Blake, R.G., Noyes, C.D., and Maley, M.: Modeling alluvial
493 fan aquifer heterogeneity at multiple scales through stratigraphic assessment. Proceedings of the
494 International Groundwater Symposium: Bridging the gap between measurement and modeling in
495 heterogeneous media, Lawrence Berkeley National Laboratory, Berkeley, California, p25-28, 2002a.

496 Weissmann, G.S., Mount, J.F., and Fogg, G.E.: Glacially driven cycles in accumulation space and
497 sequence stratigraphy of a stream-dominated alluvial fan, San Joaquin Valley, California, USA, *J. of*
498 *Sediment. Res.* 72 (2), 240-251, 2002b.

499 Weissmann, G.S., Hartley, A.J., Nichols, G.J., Scuderi, L.A., Olson, M., Buehler, H., and Banteah, R.,
500 Fluvial form in modern continental sedimentary basins: the distributive fluvial system (DFS) paradigm:
501 *Geology*, 38, 39-42, doi: 10.1130/G30242.1, 2010.

502 Weissmann, G.S., Hartley, A.J., Scuderi, L.A., Nichols, G.J., Davidson, S.K., Owen, A., Atchley, S.C.,
503 Bhattacharyya, P., Chakraborty, T., Ghosh, P., Nordt, L.C., Michel, L., and Tabor, N.J., Prograding
504 distributive fluvial systems – geomorphic models and ancient examples, in Driese, S.G., and Nordt, L.C.
505 (eds), *New Frontiers in Paleopedology and Terrestrial Paleoclimatology*, SEPM Special Publication No.
506 104, p. 131-147, 2013.

507 Wu, Y., Guo, J., and Qiang, J.: Assessing the total dissolved solid in groundwater on basis of resistivity.
 508 Conference on Groundwater Survey and Monitoring Technology, Baoding Hebei, China, 2003. (In
 509 Chinese)

510 Yang, C., Dai, Z., Romanak, K., Hovorka, S., and Trevino, R.: Inverse Modeling of Water-Rock-CO₂
 511 Batch Experiments: Implications for Potential Impacts on Groundwater Resources at Carbon
 512 Sequestration Sites, *Environ. Sci. Technol.*, 48, 2798–2806, doi: 10.1021/es4041368, 2014.

513 Yang, Y., Luo, Y., Liu, M., Wang, R., and Wang, H.: Research of features related to land subsidence
 514 and ground fissure disasters in the Beijing Plain: Prevention and Mitigation of Natural and
 515 Anthropogenic Hazards due to Land Subsidence - Proc. IX Int. Symp. on Land Subsidence, K. Daito et
 516 al. eds., Proc. IAHS,UK, 372, 239-242, 2015.

517 Yeh, T.C., Liu, S., Glass, R.J., Baker, K., Brainard, J.R., Alumbaugh, D., and LaBrecque, D.: A
 518 geostatistically based inverse model for electrical resistivity surveys and its applications to vadose zone
 519 hydrology. *Water Resour. Res.*, 38, 1278, doi: 10.1029/2001wr001204, 2002.

520 Zappa, G., Bersezio, R., Felletti, F., and Giudici, M.: Modeling heterogeneity of gravel-sand, braided
 521 stream, alluvial aquifers at the facies scale. *J. Hydrol.*, 325,134-153, doi :10.1016/j.jhydrol.2005.10.016,
 522 2006.

523 Zhu, L., Gong, H., Li, X., Li, Y., Su, X., and Guo, G.: Comprehensive analysis and artificial intelligent
 524 simulation of land subsidence of Beijing, China. *Chin. Geogra. Sci.*, 23, 237–248, doi: 10.1007/s11769-
 525 013-0589-6, 2013.

526 Zhu, L., Gong, H., Li, X., Wang, R., Chen, B., Dai, Z., and Teatini, P.: Land subsidence due to
 527 groundwater withdrawal in the northern Beijing plain, China, *Eng. Geol.*, 193, 243-255, doi:
 528 10.1016/j.enggeo.2015.04.020, 2015.

529 Zhu, L., Dai, Z., Gong, H., Gable, C., and Teatini, P.: Statistic inversion of multi-zone transition
 530 probability models for aquifer characterization in alluvial fans. *Stoch. Environ. Res. Risk Assess.*, 30,
 531 1005-1016, doi: 10.1007/s00477-015-1089-2, 2016a.

532 Zhu, L., Gong, H., Chen, Y., Li, X., Chang, X., and Cui, Y.: Improved estimation of hydraulic
533 conductivity by combining stochastically simulated hydrofacies with geophysical data. *Sci. Rep.*, 6,
534 22224, doi: 10.1038/srep22224, 2016b.

535 **Table 1 Values of the volumetric proportion for the various facies in three zones**

536

Zone	Sub-clay and clay	Fine sand	Medium-coarse sand	Gravel
Zone 1	0.166	0.234	0.067	0.533
Zone 2	0.409	0.286	0.065	0.240
Zone3	0.503	0.328	0.106	0.063

537

538

539

540

541

542

543

544

545 **Table 2 Statistical data of logarithm hydraulic conductivity ($\log_{10}(m/d)$) in the three zones of the Chaobai**
546 **alluvial fan**

Zone	Parameter	Fine sand	Medium-coarse sand	Gravel
	Mean	1.07	1.82	2.92
Zone 1	Minimum	-0.94	1.22	2.26
	Maximum	1.65	2.45	3.66
	Proportion	0.36	0.12	0.32
	Mean	0.42	1.17	2.65
Zone 2	Minimum	-2.22	-0.23	0.95
	Maximum	1.22	2.07	3.38
	Proportion	0.23	0.14	0.31
	Mean	0.17	0.81	2.48
Zone 3	Minimum	-2.64	-0.78	0.34
	Maximum	0.72	1.43	3.21
	Proportion	0.35	0.17	0.12

547

548

549

550

551 **Table 3 Optimized parameters in the fitting exponential function of $\log_{10}(K)$ semivariogram in vertical**
552 **direction for the various facies and zones**

Zone	Parameter	Fine sand		Medium-coarse sand		Gravel	
		Estimated value	Confidence Interval (95%)	Estimated value	Confidence Interval (95%)	Estimated value	Confidence Interval (95%)
Zone 1	Variance	0.23	(0.19, 0.28)	0.32	(0.29, 0.34)	1.60	(1.41, 1. 81)
	Range (m)	6.01	(2.01, 20.52)	8.01	(1.53, 14.67)	6.50	(6.5, 12.84)
Zone 2	Variance	0.069	(0.067, 0.070)	0.14	(0.13, 0.15)	1.22	(1.19, 1.24)
	Range (m)	3.13	(1.83, 4.42)	8.27	(3.61, 12.93)	15.0	(12.33, 17.67)
Zone3	Variance	0.05	(0.047, 0.053)	0.126	(0.118, 0.135)	0.62	(0.54, 0.7)
	Range (m)	6.52	(2.19, 10.85)	2.72	(0.20, 6.55)	5.98	(0.20, 15.63)

553
554
555
556 **Table 4 Variances of $\log_{10}(K)$ of different facies along the dip direction in Zone 2 and Zone 3**

Zone		Fine sand	Medium-coarse sand	Gravel
Zone 2	Estimated value	0.10	0.15	1.38
	Confidence Interval (95%)	(0.059, 0.141)	(0.071, 0.228)	(1.14, 1.62)
Zone 3	Estimated value	0.045	0.068	0.48
	Confidence Interval (95%)	(0.030, 0.0607)	(0.043, 0.093)	(0.22, 0.73)

560 **Figure captions**

561 Figure 1 Chaobai alluvial fan in the north of Beijing Plain. (a) Location of the study area and
562 distribution of the field data. (b) Map of the hydraulic conductivity issued by Beijing Institute of
563 Hydrogeology and Engineering Geology (2007). The location of the study area is shown in the inset.

564 Figure 2 Flowchart of the geostatistical methodology

565 Figure 3 Typical depth behaviors of resistivity and corresponding stratigraphy in the eastern part of
566 Zone 2

567 Figure 4 Inversed resistivity and corresponding stratigraphy in Zone 1

568 Figure 5 Experimental (circle symbol) and model (solid line) semivariogram along the vertical direction
569 for the various hydrofacies in the three zones. Notice that the range in the y-axis differs for sands and
570 gravel lithologies in Zone 2 and Zone 3.

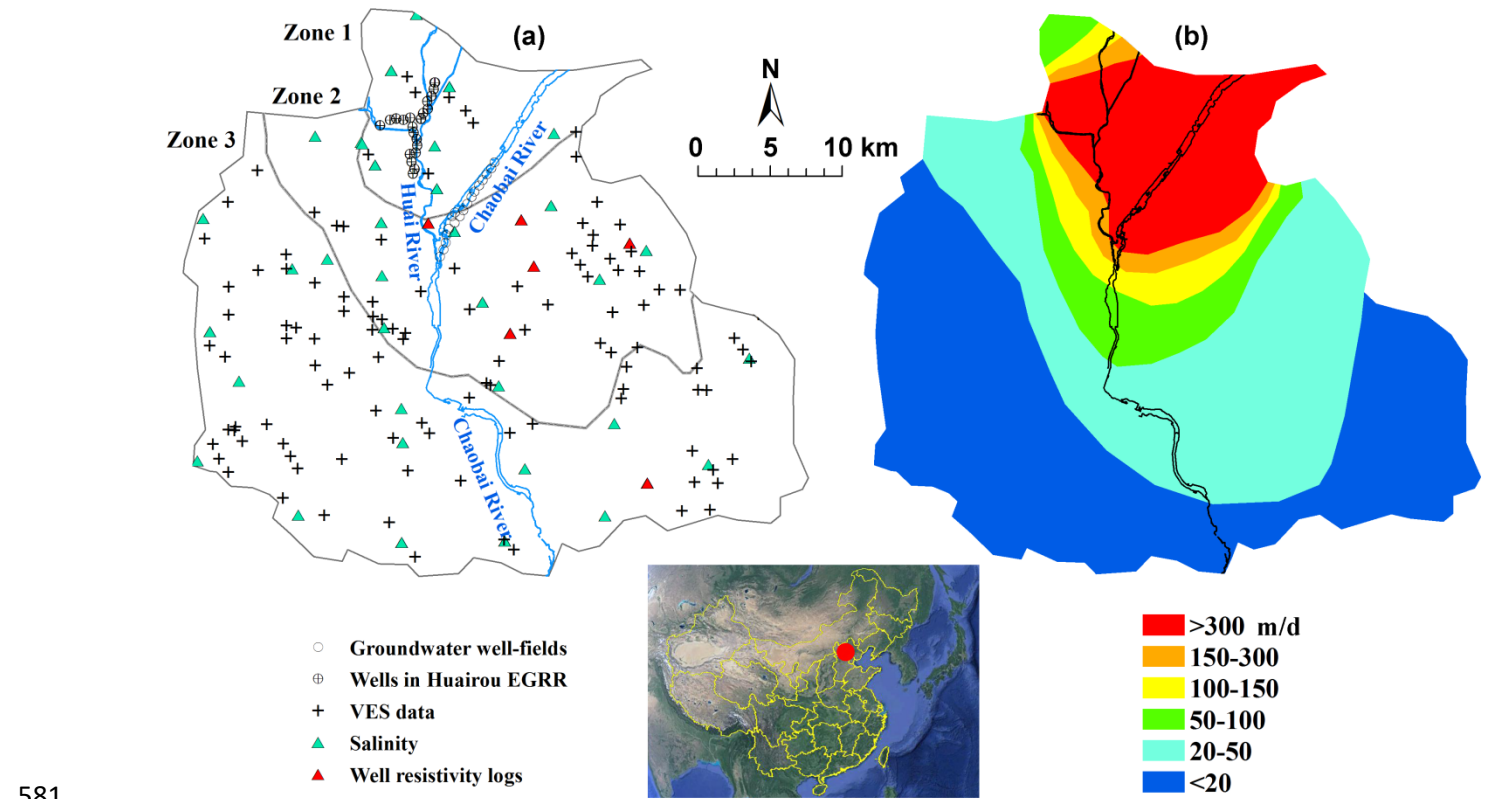
571 Figure 6 Experimental (circle symbol) and model (solid line) semivariogram along the dip direction for
572 the various hydrofacies in Zone 2 and Zone 3.

573 Figure 7 Experimental (circle symbol) and model (solid line) composited semivariogram along the
574 vertical direction for the three zones.

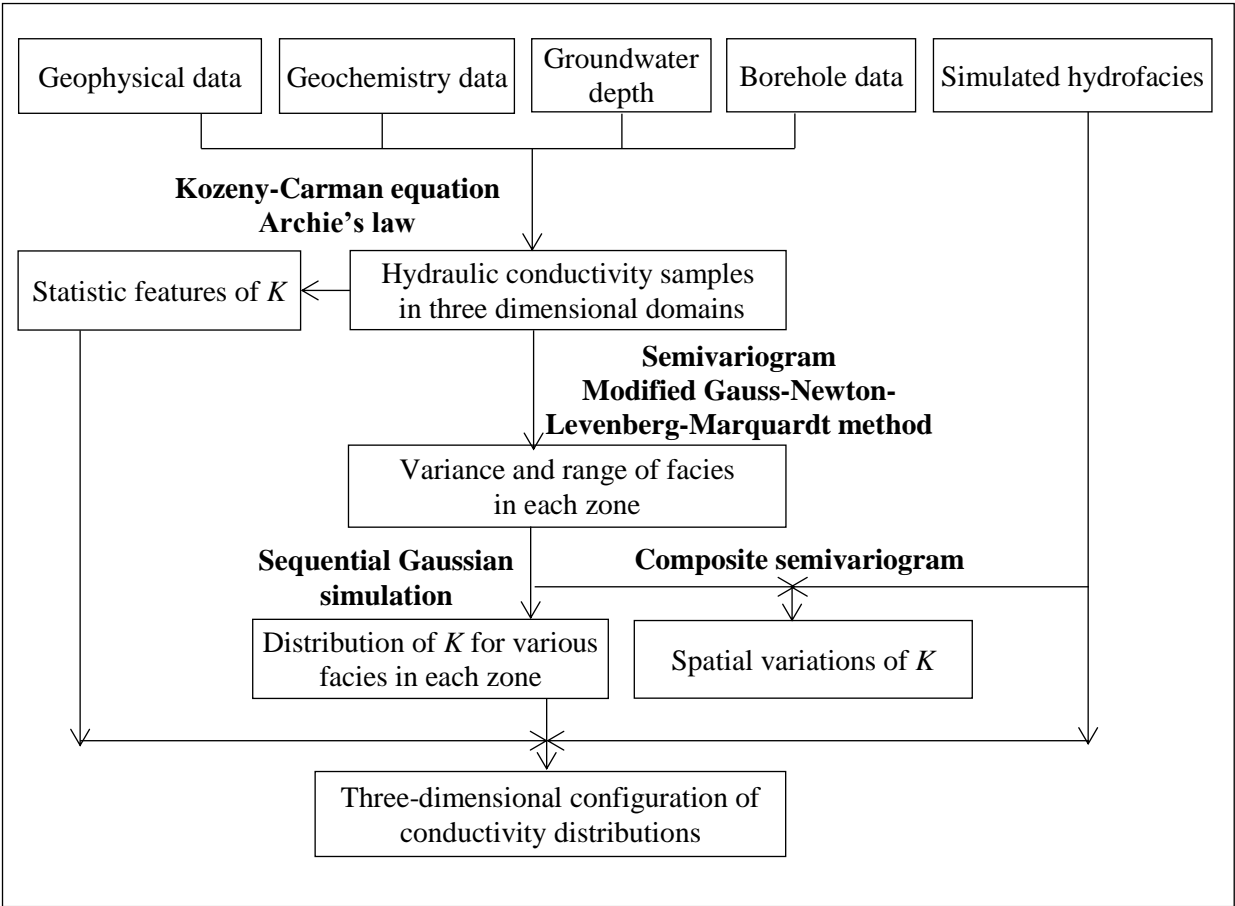
575 Figure 8 Distribution of hydrofacies (after Zhu et al., 2015a) and $\log_{10}(K)$ in the three-dimensional
576 domain representing the Chaobai alluvial fan: (a) axonometric projection of the three-dimensional
577 system and (b) vertical sections along the A-A', B-B', C-C' and D-D' alignments. The vertical

578 exaggeration is 25. The selected cell size is 300 m in north-south and east-west directions and 5 m in
 579 vertical direction, with a total number of 747, 540 cells. The thickness of the simulated domain is 300 m.

580 **Figure 1**



581
 582



589

590

591

592

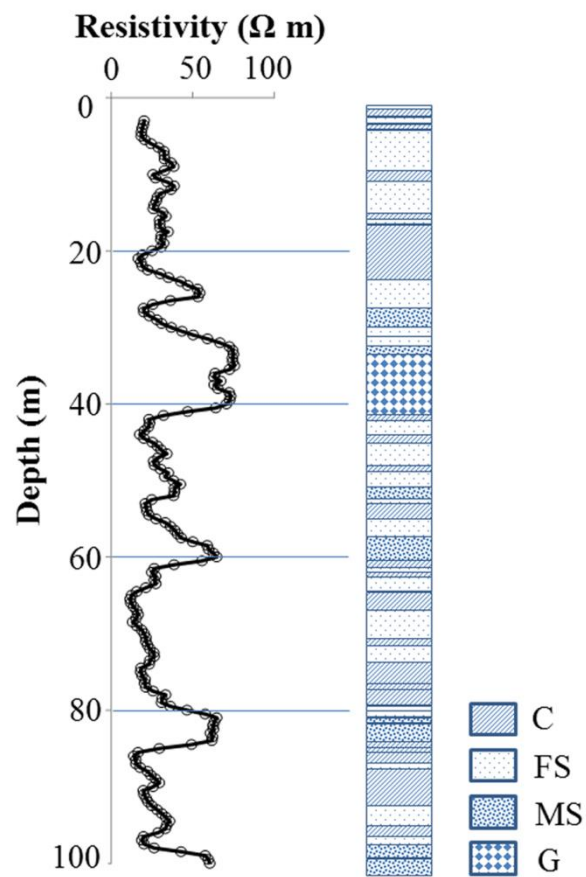
593

594

595

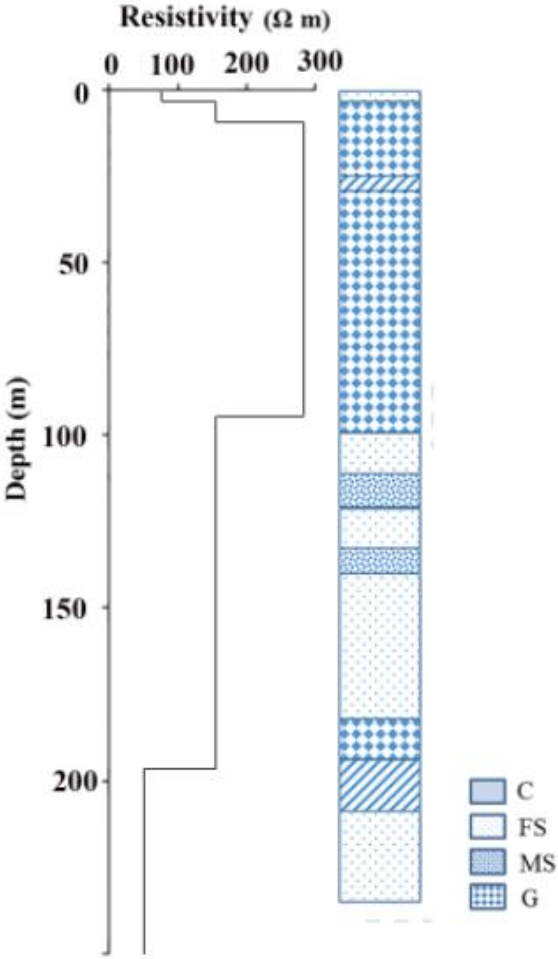
596

Figure3



597

598 **Figure 4**



599

600

601

602

603

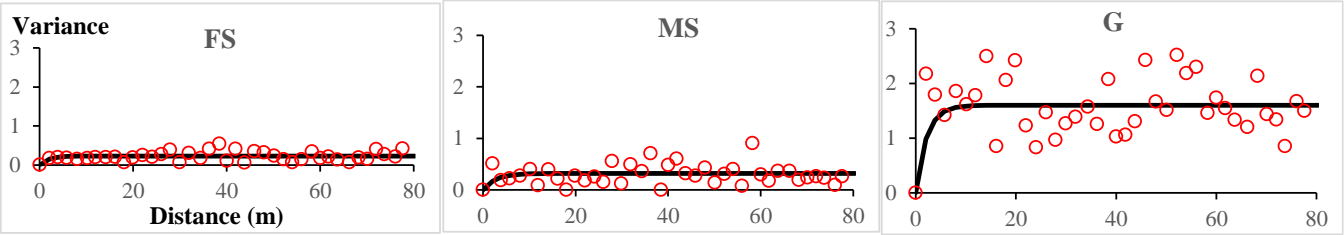
604

605

606

607 **Figure 5**

608



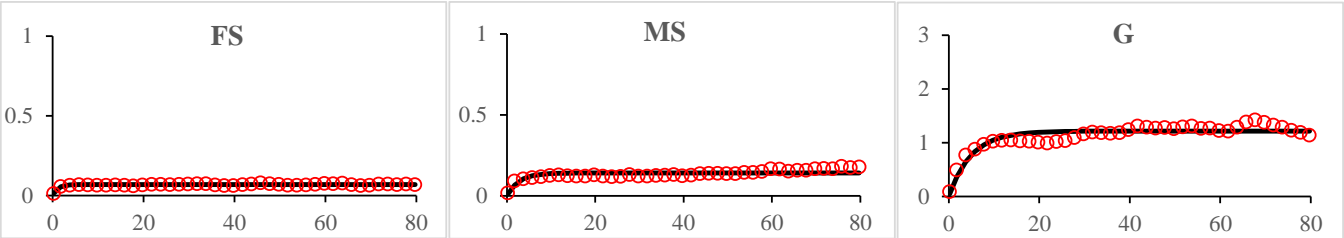
609

610

611

612

Zone1



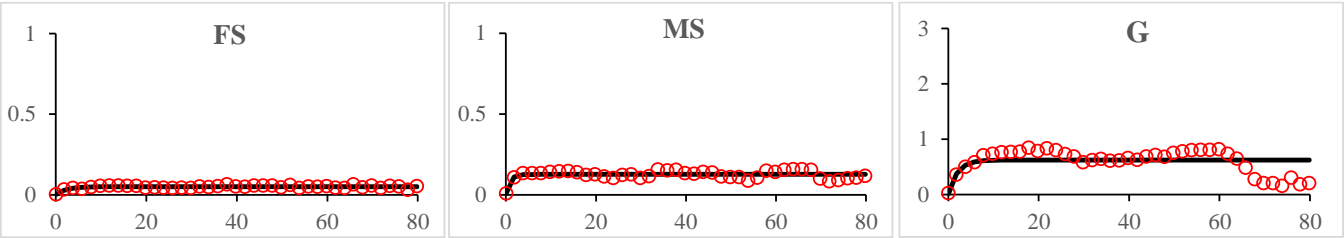
613

614

615

616

Zone 2



617

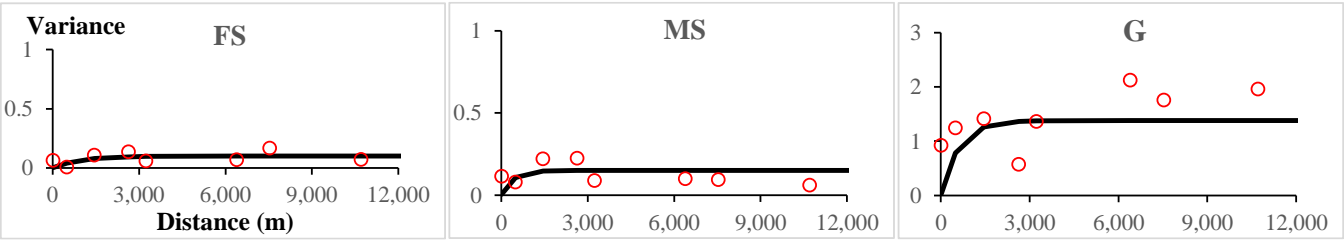
618

619

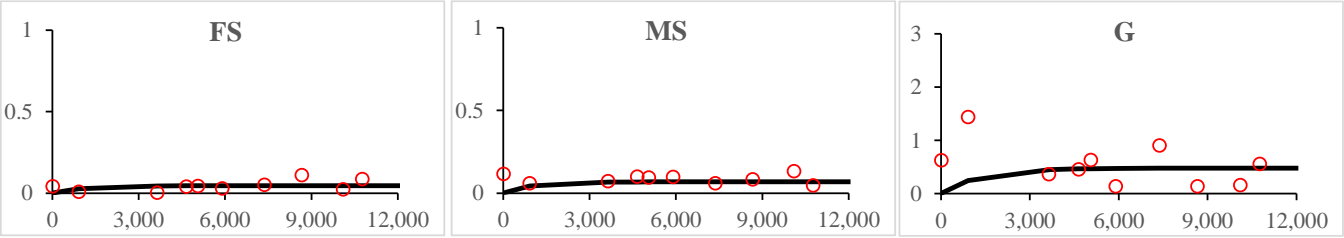
620

Zone 3

621 **Figure 6**

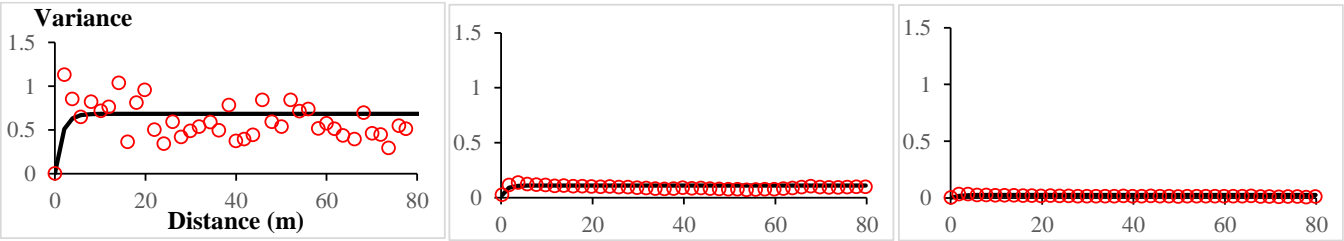


623 **Zone 2**



626 **Zone 3**

627 **Figure 7**



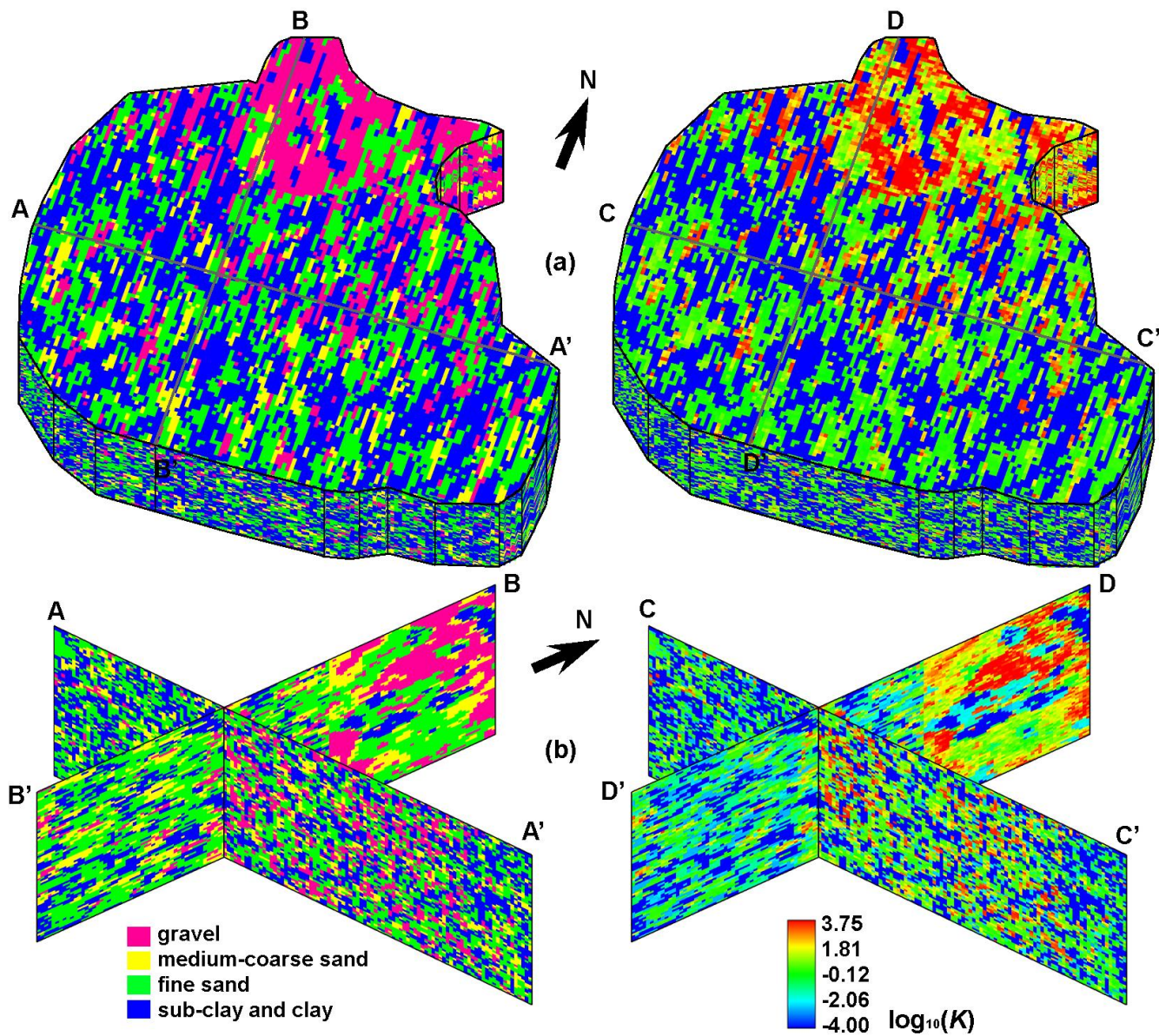
630 **Zone 1**

631 **Zone 2**

632 **Zone 3**

634

635 **Figure 8**



636

637